PAPER • OPEN ACCESS

Large-area patterning for broadband, quasi-omnidirectional low-reflectance glass

To cite this article: Brian D Jennings *et al* 2022 *J. Micromech. Microeng.* **32** 085009

View the article online for updates and enhancements.

You may also like

Large-area patterning for broadband, quasi-omnidirectional low-reflectance glass

Brian D Jennings[1,2,*] ⓘ, **Riley Gatensby**[1,2], **Elsa C Giraud**[1,2], **Andrew Selkirk**[1,2] ⓘ, **Sajjad Husain Mir**[1,2] **and Parvaneh Mokarian-Tabari**[1,2,*]

[1] Advanced Materials and BioEngineering Research Centre (AMBER), Trinity College Dublin, Dublin 2, Ireland
[2] School of Chemistry, Trinity College Dublin, Dublin 2, Ireland

E-mail: brjennin@tcd.ie and Parvaneh.Mokarian@tcd.ie

CrossMark

Abstract

A method for producing large-area, broadband, quasi-omnidirectional low-reflectivity glass surfaces is presented. Using block copolymer patterning and inductively coupled plasma etching, near-periodic arrays of pillars are formed in glass. The patterned surface has reflectivity <0.5%—almost an order of magnitude smaller than plain glass—with a bandwidth of ~300 nm. Substrates etched on both sides transmit >99.5% across the wavelength range 850–1200 nm, with >99% down to $\lambda = 650$ nm. The process is demonstrated on a 5 cm diameter fused silica wafer and high transmittance is maintained up to at least 70° incidence. The resulting substrates might find application as lab optics (windows, lenses, etc) display screens for televisions, computers, phones, and as encapsulants for optoelectronic devices.

Supplementary material for this article is available online

(Some figures may appear in colour only in the online journal)

1. Introduction

Anti-reflective coatings are common across lab and consumer devices. Lasers, light-emitting diodes, computer monitors, optical lenses and windows, etc have their surfaces modified to decrease reflection and improve their performance. Several methods have been developed to reduce surface reflectivity, such as thin-film coating and surface structuring [1–5].

Thin films decrease the amount of reflected light by taking advantage of destructive interference and can thus yield nil reflection at discrete wavelengths and angles. However, coatings of many individual films are required to achieve broadband and omnidirectional anti-reflectivity. Each film in a coating must have its refractive index in between that of the substrate and the ambient and thus a large range of materials can be required for the coatings to be effective over a significant bandwidth. Porous layers formed by leeching or by coating have also been demonstrated as films of adjustable refractive index [2, 6–8]. Surface structuring is an alternative method whereby structures (typically sub-wavelength) are formed on the surface of the substrate either by etching or by coating [5, 9–12]. These protuberances cause the refractive index to vary from ambient to substrate. By deliberate shaping of the structures, a gradient refractive index (GRIN)

layer is formed. GRIN layers are known to minimise reflections over a wide band of wavelengths and a broad range of angles [3, 13, 14]. These types of surfaces have been found in natural, biological entities such as moths' eyes and the wings of certain butterflies and have extremely low reflectivity [15–17]. Techniques such as nano-imprint lithography, laser interference lithography, rapid thermal annealing, direct etching and others have been used to fabricate nano-scale structures [18–29]. However, these processes struggle to combine good periodicity, large-area patterning and deeply sub-micron resolution while maintaining scalability and minimising cost-vs-throughput. Block copolymer (BCP) patterning is an emerging nanopatterning technique which has recently gained interest in the photonics community because it can produce nanoscale features on both curved and flat surfaces with uniformity over large areas without the requirement of stitching [30–33]. BCPs have the capability to produce well-defined nanoscale features over macroscale areas (2″ wafer [34, 35]; 12″ × 3″ substrate [36]; 4″ wafer [37]; here, we demonstrate 5 cm diameter) and, further, can define periodic patterns—advantageous in many photonic applications. BCP patterning has been demonstrated on a variety of substrates and with numerous materials incorporated in the pattern.

BCP patterning is recognised as a promising approach for nanofabrication [38–42]. BCP self-assembly can generate periodic arrays of microdomains with versatile morphology and regular feature size in the range 5–100 nm, driven by minimisation of free energy of the BCP system. The dimensions and morphology of the arrays can be tuned in a number of ways, such as: (a) control volume fraction (f) of one of the segments; (b) segregation strength (χN), where N is the overall degree of polymerisation and χ is the Flory-Huggins interaction parameters, which measures the thermodynamic compatibility between the two segments [43]; and (c) performing solvent vapour annealing (SVA) can facilitate self-assembly of the BCP into specific (periodic) morphologies (lamellar, hexagonally packed cylinders, gyroids, and spheres) [44, 45]. BCP patterning has been used to produce uniform and nanoscale features in arrays on wafer scale [34–37]. Using suitable chemistry, one of the polymer domains can be selectively infiltrated with a given compound to achieve a desired functionality [41, 46]. In this work, high molecular weight (MW) 793 kg mol^{-1} polystyrene-*b*-poly(vinyl-pyrridine) (PS-*b*-P2VP) is used to form the domains and nickel oxide is then incorporated and used as an etch mask. Higher MW can give thicker films and larger feature sizes, meaning there is more material in the etch mask so it can survive a longer or stronger etch and produce taller pillars. Having taller pillars and larger periods extends the anti-reflective effect to longer wavelengths [13, 47] thus this work focuses on improving transmission for red and near-infrared wavelengths. These larger structures and spacings could also find use as diffractive optical elements.

The elimination of reflection as a result of surface structuring has been demonstrated by a few groups in recent years. Liapis *et al* achieved high transmission of fused silica (FS) substrates across the visible spectrum (peak of 99.8% at $\lambda = 656$ nm) using a method similar to the one described here [11]. The size of the structures made them suitable for visible wavelengths, however, and the transmission dropped below 99% approaching 1 μm wavelength. Busse *et al* created random anti-reflective surface structures using a direct etch method on FS and demonstrated broadband transmittance >99.5% in the range 775–1350 nm at normal incidence but did not report measurements of non-normal incidence [24]. Surface structures have also been found to have higher laser induced damage thresholds than traditional thin-film coatings [48, 49]. The aim of this work was to develop a technology that can be scaled up to produce large-area surfaces with low reflectivity over a broad range of wavelengths—spanning the visible and near-infrared spectra—and a wide range of angles. Here we show ultra-low reflectance of 5 cm FS wafers patterned with conical pillars on the front and back surfaces. Transmittance >99.5% across the wavelength range 850–1200 nm (and >99% from 650 to 1550 nm) was demonstrated at normal incidence and high transmittance was maintained for angles of incidence (AOI) up to 70°. This work goes beyond previous research by extending antireflective performance in the near infrared. Previous work using BCP patterning achieved transmittance >99% for wavelengths 400–1000 nm [11]. Here, by using high MW BCPs in forming the etch mask, transmittance >99% is maintained from 650 to 1550 nm. This work demonstrates that optical quality components can be fabricated using HMW BCPs.

2. Experimental section

2.1. Simulations

Prior to fabricating samples, different surface structures were simulated to provide insight into any suitable design parameters or targets. A height range of 50–500 nm was used and was based on the durability of the etch mask in the inductively coupled plasma (ICP) etch process. The pillars were positioned on a hexagonal close-packed (HCP) lattice with a period of 160 nm to match the pattern formed with the high MW PS-*b*-P2VP used in this work. The pillar shape was a truncated cone and the tip and base diameters of the pillars were varied independently in the ranges 10–80 nm and 80–160 nm, respectively, as these profiles were deemed achievable by fine-tuning of the etch process. Simulations were performed in MATLAB® using the rigorous coupled-wave approximation (RCWA) method in GD-Calc [50, 51]. RCWA is a relatively fast method designed for and based on periodic arrays and the trends observed in simulation provided direction for the final structure to be achieved by the etching process. Some additional information on the simulation can be found in the supplemental document.

The wavelength range used in simulations was 400–1500 nm, covering the visible spectrum and part of the near infrared and the incident angle was varied from 0° to 60°. The refractive index values for FS were taken from Malitson [52]. The reflectivity of a single surface—for a beam travelling from air to glass—was calculated and it was assumed that the lowest reflectivity in this configuration would perform well for the beam travelling from glass to air.
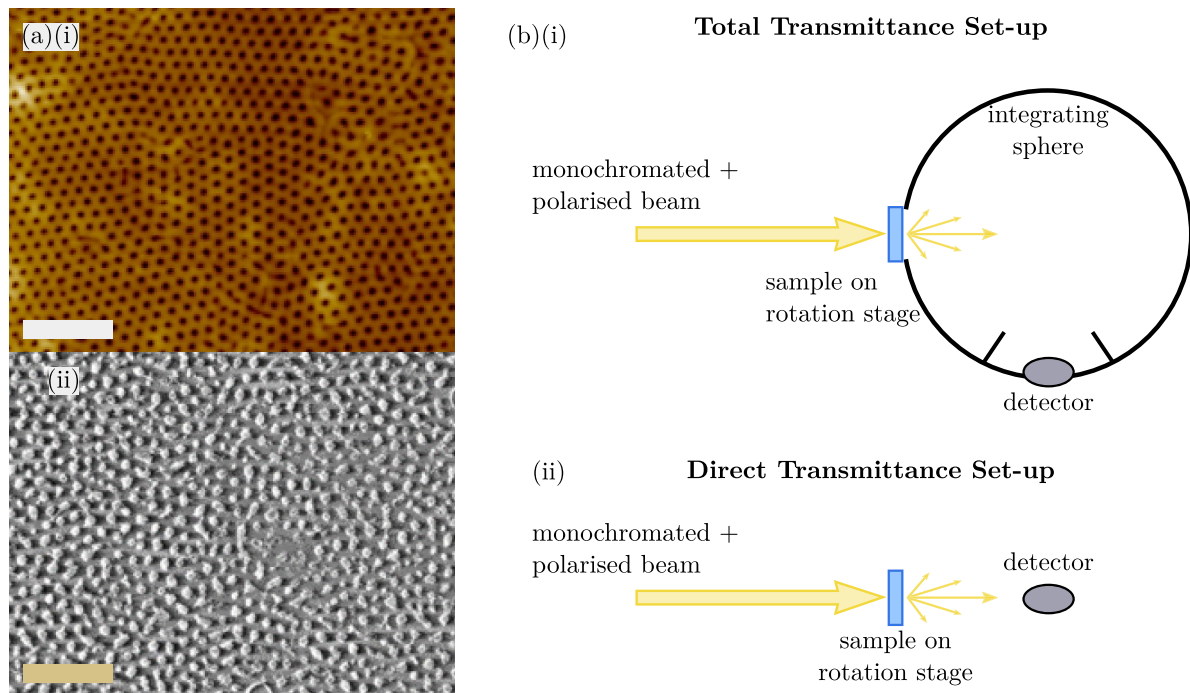
Figure 1. (a) Etch mask fabrication. (i) AFM image of BCP film after solvent vapour annealing showing P2VP cylinders (dark spots) in a PS matrix and (ii) SEM image of nickel oxide dots after polymer removal. Scale bars are 1 μm. (b) Simplified experimental set-ups for (i) total and (ii) direct optical transmittance measurements.

2.2. Block copolymer patterning

The BCP pattern was made using commercially available (from *Polymer Source*) high MW poly(styrene-*b*-2-vinylpyridine) (PS_{440}-*b*-$P2VP_{353}$) of around 793 kg mol^{-1}. Clean FS substrates (from *University Wafer*) type JGS2—2 cm $\times$ 2 cm for single-sided samples and round, 5 cm diameter for double-sided samples and 0.5 mm thick in all cases—were spin-coated with 2 wt% PS-*b*-P2VP in 4:1 toluene:tetrahydrofuran (THF) at 4500 rpm for 30 s. The BCP film was then solvent vapour annealed in a closed jar containing a mixed solvent of 2:1 THF:CHCl$_3$ for 105 minutes at room temperature to cause phase separation. The phase separated BCP film formed P2VP cylinders in a HCP lattice within a PS matrix (figure 1(a)(i)). The samples were then placed in a jar containing ethanol solvent for 45 minutes at 40°C to cause swelling of the film. At this point, nickel was incorporated into the P2VP domains by spin coating (3000 rpm, 30 s) a 0.6 wt% nickel nitrate salt (from *Fischer*) in ethanol. Oxygen plasma was used to remove the matrix polymer forming a hard mask of nickel oxide dots on the FS surface. Nickel oxide dots of average diameter 85 $\pm$ 5 nm and period 165 $\pm$ 5 nm were obtained (see figure 1(a)(ii)). After pattern transfer on one side, the above process was repeated to pattern the etch mask on the second side of the sample. The quality, coverage and dimensions of the BCP film and nickel oxide dot pattern were similar to the first side patterning.

Having produced the hard mask, samples were then etched using an Oxford PlasmaLab 180 ICP etch tool. The etchant supply was a mixture of CHF$_3$ and O$_2$. The pressure, gas composition, and source powers were varied in order to create

an optimised etch recipe. After etching, any remaining nickel oxide was removed by a nitric acid wash and the removal was confirmed by XPS measurements. Scanning electron microscopy (SEM) images of a substrate after etching are shown in section 3. Images were taken with a Zeiss Ultra SEM in both plan-view and at 70°.

2.3. Optical measurements

Measurements of total transmittance were performed with a PerkinElmer LAMBDA 1050 UV–Vis-NIR with an integrating sphere. Samples were placed at the entrance port to the integrating sphere so that all the transmitted light was collected (see figure 1(b)(i)). Total transmittance is a measure of all the light that passes through the sample, so it is only reduced by reflections or absorption (absorption is negligible for FS in this wavelength range other than near 1400 nm). Direct transmittance measures only the light that passes straight through the sample, so it is also reduced by scattering. Scans were run on the wavelength range 360–2100 nm with steps of 10 nm and the integration time was 0.6 s. Scans were repeated at least three times per sample at different positions. For measurements on the single-side patterned samples which were 1 cm $\times$ 1 cm (samples were split in half before and after etching so that processing steps could be monitored), a lens was used to reduce the spot size to a diameter of 3 mm. For the angular measurements on all samples, an adjustable aperture was placed in the beam path to achieve the same. When using the adjustable aperture, the integration time was increased to 0.8 s. Individual measurements with the unaltered beam naturally

averaged over a relatively large area because it had a spot size of 6 mm × 15 mm.

Measurements of direct transmittance were taken using a Cary 50 scan UV–Vis. Samples were placed 6 cm from the detector so that the diffuse transmittance was not collected by the detector. Scans were run on the wavelength range 360–1000 nm with steps of 5 nm and the integration time was 0.25 s. Scans were repeated at least three times per sample at different positions.

For angular measurements, a manual rotation stage was used to align the sample. The stage had 2° between markings implying some uncertainty in the measured AOI. Measurements were taken in 10° intervals from normal incidence up to a maximum angle of 60° and 70° for single- and double-side patterned samples, respectively. The maximum angle was limited by the beam encompassing the sample. A Glan-Thompson polariser (*Thorlabs*) was used to linearly polarise the light source when taking angular measurements. Measurements were taken with *s*-polarised and *p*-polarised light and subsequently averaged.

3. Results and discussion

From simulations, it was found that a conical pillar shape outperformed cylindrical for reducing reflection over a broad range of wavelengths and a wide range of angles. Better performance (i.e. lower reflection) was generally achieved by having a narrower tip diameter (d_t), a wider base diameter (d_b) and greater height (h_p); although, increasing h_p above 400 nm did not significantly improve the performance in the wavelength range under consideration. Increasing d_b while keeping the pitch fixed means that the space between pillars (at the base) reduces and thus there is a smaller step in refractive index from pillar to substrate. A narrower d_t has a similar effect at the air-pillar interface, while taller pillars allow for a more gradual change of refractive index between tip and base. A sample of the data is given in figure 2. The structures produced here would work for the near infrared and long visible wavelengths because performance drops off at shorter wavelengths where diffraction effects set in for periods larger than about $\lambda/(2\,n_s)$—where λ is the free space wavelength and n_s is the refractive index of the substrate.

The data shown in figure 2(a) are suggestive of thin film interference where reflections from the air-pillar interface interfere with reflections from the pillar-substrate interface giving rise to distinct peaks and troughs in the calculated reflectivity. For this base and tip diameter ($d_b = 100$ nm and $d_t = 80$ nm, respectively) low reflectivity could be achieved for a narrow range of wavelengths and the range could be varied by changing the height of the pillars. For figure 2(b), d_b was increased to 120 nm and d_t reduced to 40 nm. It can be seen that this reduced reflectivity at shorter wavelengths and also gave lower reflectivity in the trough regions (each graph in figure 2 is on the same colour scale). In figure 2(c), d_t was reduced to 20 nm with a d_b of 160 nm, meaning that adjacent pillars touched at the base, and this produced further reductions of the reflectivity at shorter wavelengths. It can be seen that an array of pillars with the dimensions used for figure 2 would reflect an average of roughly 0.16% over the wavelength range 400–1000 nm and beyond for pillar heights >250 nm. This gave the guidelines for the etching to produce (i) a tip diameter <40 nm, (ii) to have the bases of adjacent pillars touching and (iii) to have a pillar height of >250 nm to cover the visible wavelength range. Samples were fabricated for experimental measurement using the procedure described in section 2. Variations in reflectance intra-sample and inter-sample made it difficult to directly compare with the simulations; however, certain conclusions were drawn from the samples and additional measurement data is given in a supplemental document.

Patterned substrates (see figure 1(a)) were etched under a variety of conditions to produce a range of pillar heights and were then measured in two transmittance set-ups (see figure 1(b)). Further details are given in section 2. A sample of the etched substrates is shown in figures 3(a)–(c). There was some variation in height on individual samples, which is believed to have been caused by incomplete masking. A histogram of measured heights is given in figure S1. Total transmittance measurements taken at normal incidence showed that the patterned samples greatly increased the transmittance of the glass compared to a sample of unpatterned FS (see figure 3(d)). The data plotted for unpatterned FS was averaged over four wafers. Initially, measurements were made on samples which had been patterned on only a single side. The improvement was achieved over the entire measured range (360–2100 nm) and, depending on the sample, peaked somewhere between 600 nm and 1100 nm, see figure 3(d). Total transmittance greater than 96% was achieved over a bandwidth of more than 400 nm by the single-side patterned samples with pillar heights 270 ± 65 nm and 400 ± 95 nm. These samples come close to the maximum theoretical transmission for a single air-glass interface which was calculated from the transmission of unpatterned FS (dashed line in figures 3(d) and (e)). The height of the pillars was measured from SEM images and was found to vary slightly across the sample surface, hence the uncertainty in quoted heights. From these two samples alone, it would appear that taller pillars improve the transmission at longer wavelengths but do not perform as well as shorter pillars at shorter wavelengths. The supplementary information section contains a comparison of optical performance versus pillar height for a larger set of samples (see figure S2). It might be expected that taller pillars are needed to reduce reflection at longer wavelengths because the gentle gradient index change needs to be maintained. It is not so clear, however, that taller pillars would hinder transmission at shorter wavelengths. We believe it is due in the main to defects in the etch mask combined with the period of the etch mask. Any defects which do not result in pillars during the etch process leave a large gap and/or isolated pillars, causing scattering; as the etch time (/pillar height) increases so too does this effective roughness and thus the scattering—this type of scattering is greater for shorter wavelengths and that is why there is a fall-off in transmission.

In figure 3(d), it can be seen that transmission was increased by as much as 2.7% by patterning a single side. This is a very strong improvement as the calculated maximum possible
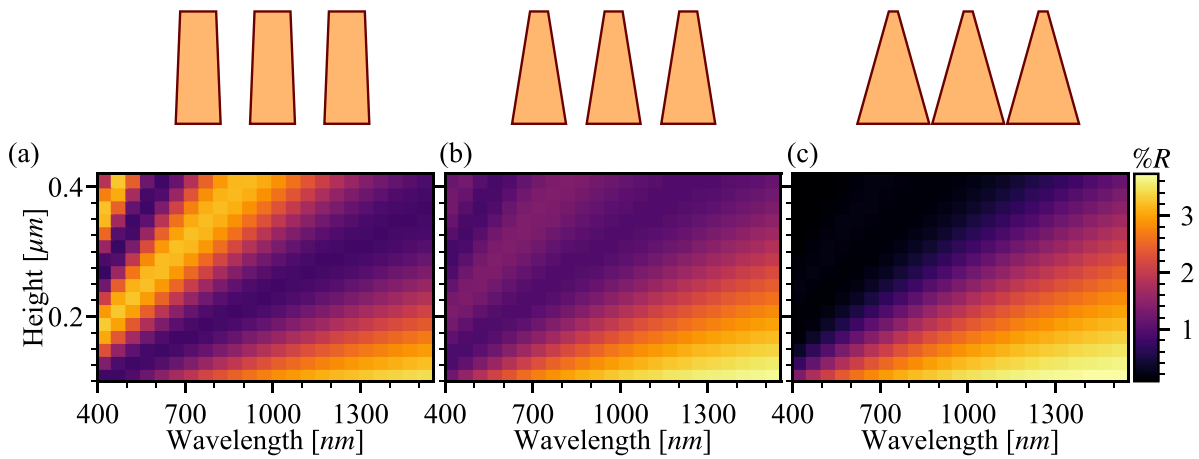
Figure 2. Calculated reflectivity of a single air-glass interface. The glass surface is covered in an array of pillars on a HCP lattice with a 160 nm period. The pillar bases are (a) 100 nm, (b) 120 nm, (c) 160 nm in diameter and tips are (a) 80 nm, (b) 40 nm, (c) 20 nm in diameter. The pillars' geometries are illustrated above the graphs.
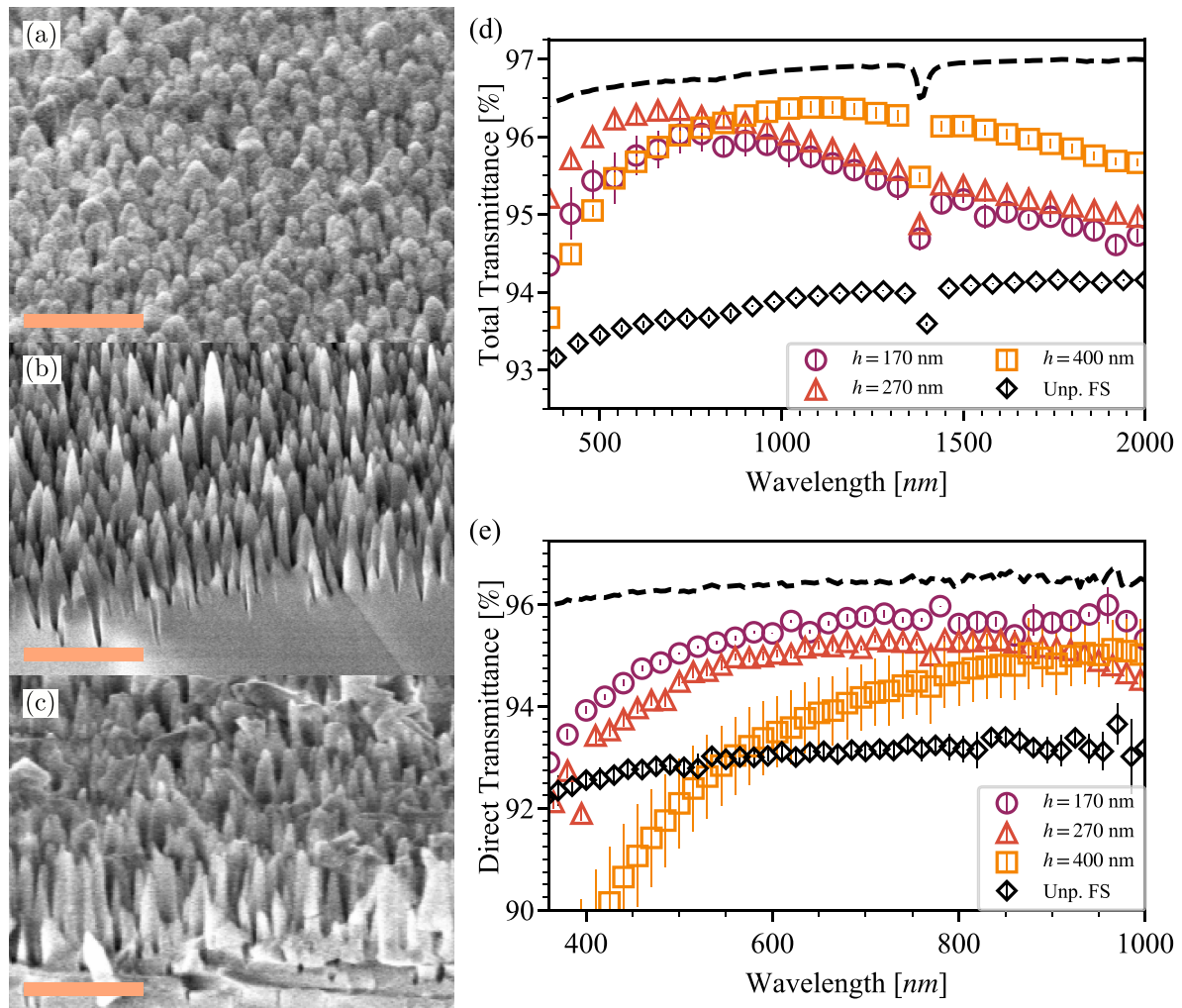

Figure 3. Angled SEM images of substrates etched on a single side with nominal pillar heights of (a) 170 nm, (b) 270 nm and (c) 400 nm. Scale bars are 500 nm. (d) Total and (e) direct transmission at normal incidence of FS patterned on one side. Samples match those shown in (a)–(c) and are compared to unpatterned FS, dotted line signifies calculated transmission for a single air-FS interface. Error bars mark one standard deviation.
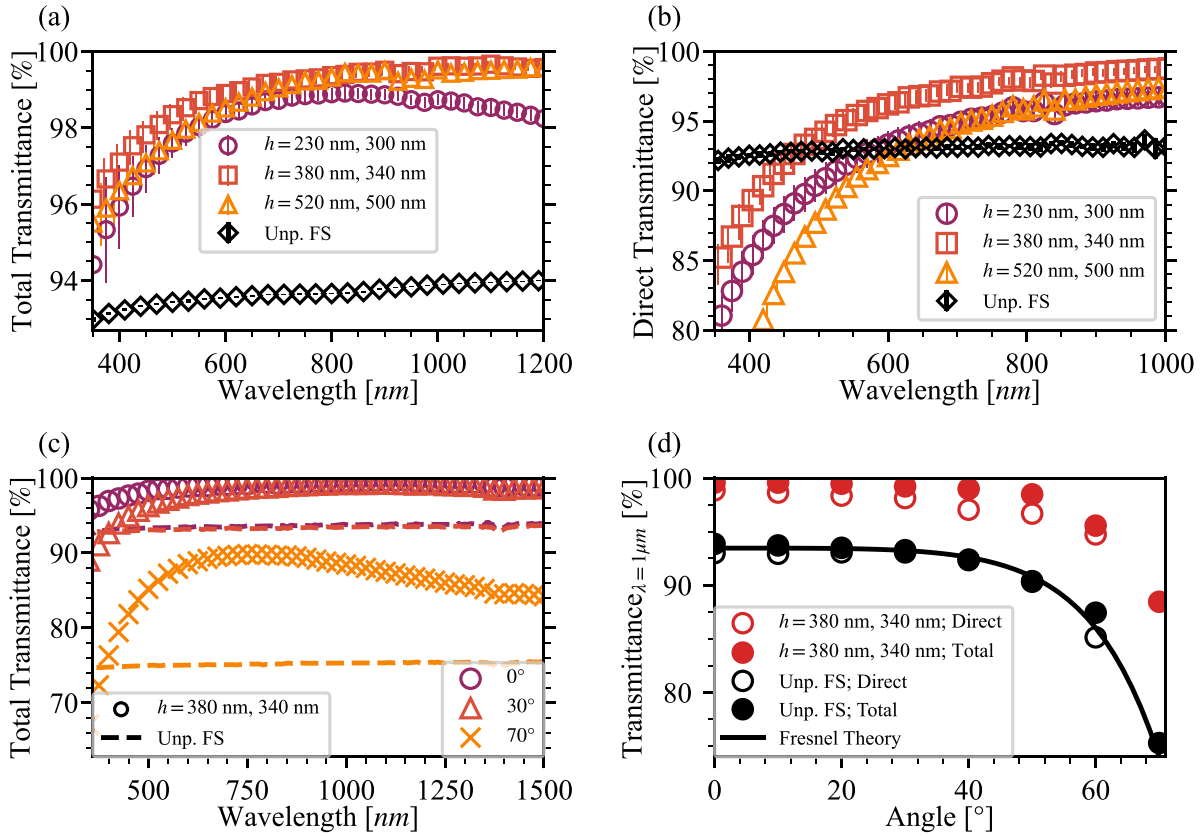
Figure 4. (a) Total and (b) direct transmission of 5 cm FS wafer patterned on both sides. Measurements were taken at normal incidence and samples are differentiated by the typical pillar height (similar on both sides). Unpatterned FS is plotted for comparison. (c) Total and (d) direct transmission at different angles of incidence for sample $h = 380$ nm compared to unpatterned FS, markers and dashed lines respectively.

increase for this FS would be ∼3.3%. The transmittance dip at 1350 nm is caused by OH groups present in the FS due to the production process. The transmission of a single surface was calculated using the measurement data of the unpatterned substrate and is plotted as a dotted line. Samples with high direct transmission are therefore necessary when it is desirable to maintain the beam's shape, such as for laser optics, while high total transmission would be sufficient when simply looking to reduce reflections. Between samples $h = 400$ nm and $h = 270$ nm the real major difference is the pillar height; the pillar spacing (and coverage) are consistent, the top and base radius are similar, however, inspection of $h = 400$ nm shows some defects lying on top of the pillars in certain areas which are expected to be broken pieces of other pillars (see figure 3(c)). It is not certain whether these defects were present before transmittance measurements or were produced while preparing the substrate for SEM imaging. The defects are believed to be part of the reason for reduced performance of $h = 400$ nm at shorter wavelengths. The data show that broadband low-reflection can be achieved in the visible and near infrared, and that the operating range can be tuned by varying the height of the pillars.

The direct transmission (see figure 3(e)) of patterned FS was also higher than unpatterned FS although, compared with total transmission, the improvement was confined to smaller ranges of wavelengths (which varied sample-to-sample).

It was seen that even relatively short pillars (165 nm, roughly one quarter of the wavelength of maximum transmission) can drastically improve the direct transmission and in fact outperform the taller pillars. Comparing figure 3(d) with (e), it can be seen that the samples which had higher total transmission had lower direct transmission. A comparison of diffuse-to-total transmission is given in figure S3. This was attributed partly to missing pillars in the surface array as a result of defects in the etch mask and to an exaggeration of defects caused by the etching of taller structures thus leading to increased scattering which is enhanced for shorter wavelengths. It is our belief that increasing the transmission of the patterned samples in the visible range further would come from improving the homogeneity of the etch mask or by having a smaller period of the mask.

The total transmittance of FS which was patterned on both sides is plotted in the graph in figure 4(a) and the improvement compared to unpatterned FS is substantial. The three samples shown had different etch durations but were otherwise fabricated under identical conditions. The etch duration was kept constant for the front and back surface on each sample in order to keep the pillar heights similar on both sides. The substrates used here were 5 cm wafers and there was only slight variation in transmission across the substrate (the absolute deviation from the mean for the six measurements taken on sample $h = 380$ nm is plotted in figure S4). Each sample achieved

close to or above 99% total transmission at normal incidence. Of these samples, pillar heights of ∼380 nm resulted in the best performance with >99.5% transmission across the wavelength range 850–1200 nm. Similar to samples patterned on a single side, it appears that having taller pillars redshifts the peak transmission. The measured transmission implies a reflectance of <0.5% which is a reduction of more than one order of magnitude compared to unpatterned FS. The samples patterned on both sides also had higher direct transmission than unpatterned FS (see figure 4(b)) for longer wavelengths. Here, the $h = 380$ nm performed best, having higher transmission than unpatterned FS for wavelengths longer than ∼500 nm, and was approaching 99% transmission near 1000 nm. This corresponds to a relative increase of ∼80%. As before, the patterned samples had lower direct than total transmission and, again, this was ascribed to scattering.

The increased transmittance is a result of the surface structuring. For most wavelengths that were measured, the structures and spacing are deeply subwavelength and thus can be approximated by an effective medium. This effective medium has a gradually varying refractive index from the top of the layer to the bottom because of the increasing diameter of the pillars and this gradient is known to greatly reduce reflection. For wavelengths approaching the separation of the structures, the effective medium is no longer a suitable description. Here, scattering will set in and this is seen in the decrease in direct transmittance at shorter wavelengths. In this size-wavelength regime, forward scattering dominates and so, high total transmittance is maintained. As the wavelength decreases further, the amount of scattering increases so that backscattering becomes significant and the total transmittance drops off as well.

Studies have predicted that the wavelength of maximum transmission and perhaps the maximum transmission value itself depend on the height of the pillars [47, 48]. There were not enough samples in this study for statistical significance to be given to any trends; however, rudimentary investigations of such a dependence were made (see figure S2) and it is planned to continue these investigations in future work.

To test the directionality of these samples, measurements of transmission were made at different AOI. It was found that the patterned samples maintained higher transmission than unpatterned FS even for large AOI (see figures 4(c) and (d)). The direct transmission of the double-side patterned sample reduces gradually as the AOI increases, at a lower rate than unpatterned FS up to at least 60°. The decline in transmission at lower wavelengths (⩽500 nm) is exaggerated as the AOI increases. However, very high transmission is maintained towards the near infrared and the patterned sample has higher transmission at 60° AOI than the unpatterned FS has at normal incidence. There is a similar trend in total transmission. Here, because of the larger measurement range, it can be seen that increasing the AOI decreased the bandwidth of transmission-a narrower range of maximum transmission emerged. The decline was slower on the long wavelength side. Despite this, the patterned FS still had significantly higher transmission across a vast range of wavelengths. For an AOI of 70°, the unpatterned FS transmitted ∼75% at a wavelength of 750 nm while the

patterned sample transmitted ∼90%. This is an increase of ∼15%, corresponding to transmission losses reducing by more than half. It should be noted that at large AOI there was a gap between the sample and the integrating sphere so part of the diffuse transmission would not have been collected in the total transmission measurements.

The high values of total transmission confirm that the samples have low reflection. For wavelengths ⩽600 nm, a considerable portion of both the transmitted and reflected light is diffuse (see SI). Thus, the performance of the samples could be improved by reducing scattering which might be achieved by fully optimising the etch mask or by using a BCP system with a smaller period. This demonstrates that broadband, multidirectional ultra-low reflection can be achieved in the visible and near infrared by surface structuring through BCP patterning with high MW systems. This advances previous work by extending the substrate size and wavelength range and furthers the case for BCP patterning as a candidate for AR functionalising. As is, the samples would be suitable as coverglasses for photoresponsive cells where the diffuse nature of the transmission may prove beneficial.

4. Conclusion

A method for producing low reflectivity FS glass by BCP patterning was demonstrated. Using high MW PS-*b*-P2VP and metal salt inclusion an etch mask was formed and the pattern was transferred to the FS substrate by ICP etching. Simulations predicted that an array of pillars with tip diameter <40 nm, bases touching and pillar height >250 nm would reflect <0.2% over the wavelength range 400–1000 nm and beyond. The resulting surface of densely-packed, conical pillars increased transmittance to >99.5% at normal incidence and maintained high transmittance up to at least 70° incidence for a broad range of wavelengths. It was found that diffuse transmittance and reflectance was significant for wavelengths ⩽500 nm and that the highest transmittance was achieved at ∼900 nm. Optical properties were seen to vary with pillar height (which was controlled by the etch process) but further investigation is required before detailed conclusions can be drawn. Further work will focus on reducing the diffuse components of transmission and reflection and improving performance at shorter wavelengths. It is also intended to etch larger substrates and substrates with curved surfaces, e.g. lenses.

Data availability statement

The data that support the findings of this study are available upon reasonable request from the authors.

Acknowledgments

Funding

ORCID iDs

Brian D Jennings ⓘ https://orcid.org/0000-0002-9915-5453
Andrew Selkirk ⓘ https://orcid.org/0000-0002-1845-7100

References

[1] Chen D 2001 Anti-reflection (AR) coatings made by sol-gel processes: a review *Sol. Energy Mater. Sol. Cells* **68** 313–36

[2] Macleod H A 2017 Antireflection coatings *Thin-Film Optical Filters* 5th edn (Boca Raton, FL: CRC Press)

[3] Minot M J 1976 Single-layer, gradient refractive index antireflection films effective from 0.35 to 2.5 μm *J. Opt. Soc. Am.* **66** 515–9

[4] Thomas I M 1986 High laser damage threshold porous silica antireflective coating *Appl. Opt.* **25** 1481–3

[5] Xi J-Q, Schubert M F, Jong Kyu K, E Schubert F, Chen M, Lin S-Y, Liu W and Smart J A 2007 Optical thin-film materials with low refractive index for broadband elimination of Fresnel reflection *Nat. Photon.* **1** 176–9

[6] Nicoll F H 1942 New chemical method of reducing the reflectance of glass *RCA Rev.* **6** 287–301

[7] Buskens P, Burghoorn M, Mourad M C D and Vroon Z 2016 Antireflective coatings for glass and transparent polymers *Langmuir* **32** 6781–93

[8] Faustini M, Grenier A, Naudin G, Ronghua Li and Grosso D 2015 Ultraporous nanocrystalline TiO₂-based films: synthesis, patterning and application as anti-reflective, self-cleaning, superhydrophilic coatings *Nanoscale* **7** 19419–25

[9] Huang Y-F *et al* 2007 Improved broadband and quasi-omnidirectional anti-reflection properties with biomimetic silicon nanostructures *Nat. Nanotechnol.* **2** 770–4

[10] Hadobás K, Kirsch S, Carl A, Acet M and Wassermann E F 2000 Reflection properties of nanostructure-arrayed silicon surfaces *Nanotechnology* **11** 161–4

[11] Liapis A C, Rahman A and Black C T 2017 Self-assembled nanotextures impart broadband transparency to glass windows and solar cell encapsulants *Appl. Phys. Lett.* **111** 183901

[12] Rahman A, Ashraf A, Xin H, Tong X, Sutter P, Eisaman M D and Black C T 2015 Sub-50 nm self-assembled nanotextures for enhanced broadband antireflection in silicon solar cells *Nat. Commun.* **6** 5963

[13] Rayleigh F R S 1880 On reflection of vibrations at the confines of two media between which the transition is gradual *Proc. London Math. Soc.* **s1–11** 51–56

[14] Southwell W H 1991 Pyramid-array surface-relief structures producing antireflection index matching on optical surfaces *J. Opt. Soc. Am.* A **8** 549–53

[15] Clapham P and Hutley M 1973 Reduction of lens reflexion by the "moth eye" principle *Nature* **244** 281–2

[16] Bernhard C G 1967 Structural and functional adaptation in a visual system—strukturelle und funktionelle adaptation in einem visuellen system *Endeavour* **26** 79–84

[17] Siddique R H, Gomard G and Hendrik H 2015 The role of random nanostructures for the omnidirectional anti-reflection properties of the glasswing butterfly *Nat. Commun.* **6** 6909

[18] Chou S Y, Krauss P R and Renstrom P J 1995 Imprint of sub-25 nm vias and trenches in polymers *Appl. Phys. Lett.* **67** 3114–6

[19] Austin M D, Ge H, Wu W, Li M, Yu Z, Wasserman D, Lyon S A and Chou S Y 2004 Fabrication of 5 nm linewidth and 14 nm pitch features by nanoimprint lithography *Appl. Phys. Lett.* **84** 5299–301

[20] Berger V, Gauthier-Lafaye O and Costard E 1997 Photonic band gaps and holography *J. Appl. Phys.* **82** 60–64

[21] Shoji S and Kawata S 2000 Photofabrication of three-dimensional photonic crystals by multibeam laser interference into a photopolymerizable resin *Appl. Phys. Lett.* **76** 2668–70

[22] Rochon P, Batalla E and Natansohn A 1995 Optically induced surface gratings on azoaromatic polymer films *Appl. Phys. Lett.* **66** 136–8

[23] Kim D Y, Tripathy S K, Lian Li and Kumar J 1995 Laser-induced holographic surface relief gratings on nonlinear optical polymer films *Appl. Phys. Lett.* **66** 1166–8

[24] Busse L E, Florea C M, Frantz J A, Brandon Shaw L, Aggarwal I D, Poutous M K, Joshi R and Sanghera J S 2014 Anti-reflective surface structures for spinel ceramics and fused silica windows, lenses and optical fibers *Opt. Mater. Express* **4** 2504–15

[25] Lee Y, Koh K, Hyungjoo N, Kim K, Kang J-J and Kim J 2009 Lithography-free fabrication of large area subwavelength antireflection structures using thermally dewetted Pt/Pd alloy etch mask *Nanoscale Res. Lett.* **4** 364

[26] Yunfeng Li *et al* 2009 Biomimetic surfaces for high-performance optics *Adv. Mater.* **21** 4731–4

[27] Verma L K, Sakhuja M, Son J, Danner A J, Yang H, Zeng H C and Bhatia C S 2011 Self-cleaning and antireflective packaging glass for solar modules *Renew. Energy* **36** 2489–93

[28] Wang S, Yu X Z and Fan H T 2007 Simple lithographic approach for subwavelength structure antireflection *Appl. Phys. Lett.* **91** 061105

[29] Eusun Y, Kim S-C, Lee H J, Oh K H and Moon M-W 2015 Extreme wettability of nanostructured glass fabricated by non-lithographic, anisotropic etching *Sci. Rep.* **1** 9362

[30] Paivanranta B Sahoo P K, Tocce E, Auzelyte V, Ekinci Y, Solak H H, Liu C-C, Stuen K O, Nealey P F and David C 2011 Nanofabrication of broad-band antireflective surfaces using self-assembly of block copolymers *ACS Nano* **5** 1860–4

[31] Akinoglu G E, Mir S H, Gatensby R, Rydzek G and Mokarian-Tabari P 2020 Block copolymer derived vertically coupled plasmonic arrays for surface-enhanced Raman spectroscopy *ACS Appl. Mater. Interfaces* **12** 23410–6

[32] Mir S H, Jennings B D, Akinoglu G E, Selkirk A, Gatensby R and Mokarian-Tabari P 2021 Enhanced dye degradation through multi-particle confinement in a porous silicon substrate: a highly efficient, low band gap photocatalyst *Adv. Opt. Mater.* **9** 2002238

[33] Stefik M, Guldin S, Vignolini S, Wiesner U and Steiner U 2015 Block copolymer self-assembly for nanophotonics *Chem. Soc. Rev.* **44** 5076–91

[34] Tao Li, Kaiyu W, Rindzevicius T, Wang Z, Lars Schulte M S Schmidt A B and Ndoni S 2016 Wafer-scale nanopillars derived from block copolymer lithography for surface-enhanced Raman spectroscopy *ACS Appl. Mater. Interfaces* **8** 15668–75

[35] Rasappa S, Hulkkonen H, Schulte L, Ndoni S, Reuna J, Salminen T and Niemi T 2019 High molecular weight block copolymer lithography for nanofabrication of hard mask and photonic nanostructures *J. Colloid Interface Sci.* **534** 420–9

[36] Singh G, Batra S, Zhang R, Hongyi Yuan K G Yager M C, Berry B and Karim A 2013 Large-scale roll-to-roll fabrication of vertically oriented block copolymer thin films *ACS Nano* **7** 5291–9

[37] Jin H M *et al* 2017 Flash light millisecond self-assembly of high χ block copolymers for wafer-scale sub-10 nm nanopatterning *Adv. Mater.* **29** 1700595

[38] Vignolini S *et al* 2012 A 3D optical metamaterial made by self-assembly *Adv. Mater.* **24** O23–O27

[39] Kim B H, Kim J Y and Kim S O 2013 Directed self-assembly of block copolymers for universal nanopatterning *Soft Matter* **9** 2780–6

[40] Cummins C, Ross Lundy J J Walsh V P, Fleury G and Morris M A 2020 Enabling future nanomanufacturing through block copolymer self-assembly: a review *Nano Today* **35** 100936

[41] Mokarian-Tabari P, Senthamaraikannan R, Colm Glynn T W Collins C C, Nugent D, O'Dwyer C and Morris M A 2017 Large block copolymer self-assembly for fabrication of subwavelength nanostructures for applications in optics *Nano Lett.* **17** 2973–8

[42] Frascaroli J, Brivio S, Lupi F F, Seguini G, Boarino L, Perego M and Spiga S 2015 Resistive switching in high-density nanodevices fabricated by block copolymer self-assembly *ACS Nano* **9** 2518–29

[43] Albert J N L and Epps T H 2010 Self-assembly of block copolymer thin films *Mater. Today* **13** 24–33

[44] Hulkkonen H, Salminen T and Niemi T 2019 Automated solvent vapor annealing with nanometer scale control of film swelling for block copolymer thin films *Soft Matter* **15** 7909–17

[45] Sinturel C, Vayer Mène, Morris M and Hillmyer M A 2013 Solvent vapor annealing of block polymer thin films *Macromolecules* **46** 5399–415

[46] Cummins C and Morris M A 2018 Using block copolymers as infiltration sites for development of future nanoelectronic devices: achievements, barriers and opportunities *Microelectron. Eng.* **195** 74–85

[47] Carlie N 2020 Nano-structured anti-reflective surfaces from edmund optics (conference presentation) *Proc. SPIE* **11512** 1151203

[48] MacLeod B D *et al* 2017 CW laser damage testing of RAR nano-textured fused silica and YAG *Proc. SPIE* **10447** 13–25

[49] Busse L E, Frantz J A, Shaw L B, Aggarwal I D and Sanghera J S 2015 Review of antireflective surface structures on laser optics and windows *Appl. Opt.* **54** F303–10

[50] Moharam M G, Grann E B, Pommet D A and Gaylord T K 1995 Formulation for stable and efficient implementation of the rigorous coupled-wave analysis of binary gratings *J. Opt. Soc. Am.* A **12** 1068–76

[51] Johnson K C 2019 Grating diffraction calculator (gd-calc®) (available at: www.codeocean.com/)

[52] Malitson I H 1965 Interspecimen comparison of the refractive index of fused silica *J. Opt. Soc. Am.* **55** 1205–9